



Salt-Mediated Stiffening, Destruction, and Resculpting of Actomyosin Network

Bekele J. Gurmessa^{1,2}, Michael J. Rust³, Moumita Das⁴, Jennifer L. Ross⁵ and Rae M. Robertson-Anderson^{2*}

¹Department of Physics and Astronomy, Bucknell University, Lewisburg, PA, United States, ²Department of Physics and Biophysics, University of San Diego, San Diego, CA, United States, ³Department of Molecular Genetics and Cell Biology, University of Chicago, Chicago, IL, United States, ⁴School of Physics and Astronomy, Rochester Institute of Technology, Rochester, NY, United States, ⁵Department of Physics, Syracuse University, Syracuse, NY, United States

Cells dynamically change their viscoelastic properties by restructuring networks of actin filaments in the cytoskeleton, enabling diverse mechanical processes such as mobility and apoptosis. This restructuring is modulated, in part, by actin-binding proteins, such as myosin II, as well as counterions such as Mg^{2+} and K^+ . While high concentrations of Mg^{2+} can induce bundling and crosslinking of actin filaments, high concentrations of K^+ destabilize myosin II minifilaments necessary to crosslink actin filaments. Here, we elucidate how the mechanics and structure of actomyosin networks evolve under competing effects of varying Mg^{2+} and K^+ concentrations. Specifically, we couple microfluidics with optical tweezers microrheology to measure the time-varying linear viscoelastic moduli of actin networks crosslinked *via* myosin II as we cycle between low and high Mg^{2+} and K^+ concentrations. Our complementary confocal imaging experiments correlate the time-varying viscoelastic properties with salt-mediated structural evolution. We find that the elastic modulus displays an intriguing non-monotonic time dependence in high-salt conditions, that correlates with structural changes, and that this process is irreversible, with the network evolving to a new steady-state as Mg^{2+} and K^+ decrease back to their initial concentrations.

Keywords: optical tweezers, microrheology, actin, myosin, microfluidics, counterion condensation, crosslinking, bundling

OPEN ACCESS

Edited by:

Manlio Tassieri,
University of Glasgow,
United Kingdom

Reviewed by:

Davide Michieletto,
University of Edinburgh,
United Kingdom
Marco Laurati,
University of Florence, Italy

*Correspondence:

Rae M. Robertson-Anderson
randerson@sandiego.edu

Specialty section:

This article was submitted to
Soft Matter Physics,
a section of the journal
Frontiers in Physics

Received: 18 August 2021

Accepted: 25 October 2021

Published: 19 November 2021

Citation:

Gurmessa BJ, Rust MJ, Das M,
Ross JL and Robertson-Anderson RM
(2021) Salt-Mediated Stiffening,
Destruction, and Resculpting of
Actomyosin Network.
Front. Phys. 9:760340.
doi: 10.3389/fphy.2021.760340

1 INTRODUCTION

Diverse networks of semiflexible actin filaments, key components of the cell cytoskeleton, play important mechanical and structural roles in myriad cellular processes ranging from motility and division to shape change and metastasis [1–5]. To enable such diverse processes, a wide variety of actin-binding proteins (ABPs) crosslink, bundle, sever, and pull on actin filaments [6–8]. The size, shape, binding affinity and concentration of the ABP determines the resulting mechanical and structural network properties [7,9–11,11–20].

Myosin II, one of the most widely-studied ABPs [21–27], is best known for its ATP-driven restructuring of actin networks by polymerizing into minifilaments that actively push and pull on actin filaments [28–32]. However, at low ATP concentrations (≤ 1 mM), myosin II minifilaments function as passive transient crosslinkers that can also bundle actin filaments [24–27]. Microrheological measurements of actomyosin networks carried out in this limit [26,31] have

shown that myosin crosslinking leads to an increased plateau modulus and reduced stress dissipation [26].

Further, due to the polyelectrolyte nature of actin filaments, high concentrations of multivalent counterions, such as Mg^{2+} , can also crosslink and bundle actin filaments by forming counterion crossbridges [2,13,33–37]. Several studies have investigated this effect, focusing on the structural properties of actin networks formed under varying multivalent salt conditions [33,38–42]. Further, we previously showed that the plateau modulus, nonlinear stiffness, and relaxation timescales of entangled actin networks were all higher when polymerized in the presence of higher Mg^{2+} concentrations (ranging from 2 to 52 mM) [34].

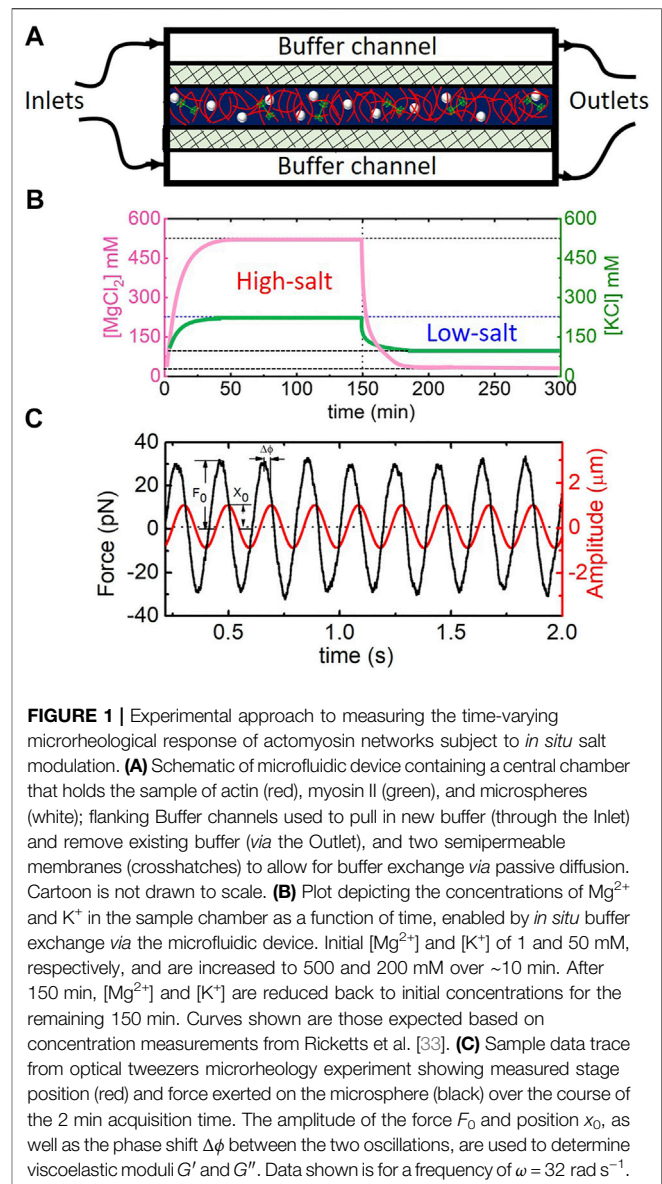
On the other hand, increasing the concentration of K^+ in actomyosin networks, can destabilize myosin minifilaments [43]. At K^+ concentrations of ~ 600 mM, myosin remains in dimeric form, but upon lowering to < 150 mM, myosin dimers assemble into minifilaments that can crosslink and bundle actin filaments and generate forces at high enough ATP concentration [30,43,44].

Here, we use time-resolved optical tweezers microrheology coupled with microfluidics to probe the time-varying viscoelasticity of steady-state actomyosin networks subject to *in situ* modulation of $[K^+]$ and $[Mg^{2+}]$ (Figure 1). Our complementary confocal microscopy experiments shed light on the structural evolution that gives rise to the non-equilibrium viscoelasticity. We find that networks exhibit first an increase then a decrease in elastic modulus with increasing $[Mg^{2+}]$ and $[K^+]$, and that this non-monotonic dependence is irreversible, with the networks transitioning to a new steady-state as the environment returns to the initial ionic conditions. We postulate that this intriguing behavior arises from a competition between salt-mediated actin bundling, which increases the modulus, and myosin minifilament depolymerization, which destroys the network connectivity and thus elasticity. While minifilament disassembly is reversible, filament bundling is not; so the network that reforms at low salt is in a new bundled state.

2 MATERIALS AND METHODS

Sample Preparation: Rabbit skeletal actin (Cytoskeleton, Inc. AKL99) and Alexa-568 labeled actin (Thermo Fisher Scientific, A12373) are stored at -80°C in G-buffer (2 mM Tris pH 8.0, 0.5 mM DTT, 0.1 mM CaCl_2 , 0.2 mM ATP). Chicken skeletal myosin II, a gift from the Kovar lab at University of Chicago, is stored at -80°C in (600 mM KCl, 25 mM KPO_4 , 10 mM EDTA, 1 mM DTT). Before experiments, myosin is dialyzed against 300 mM KCl in a 96-well 10 kDa MWCO microdialysis plate (ThermoFisher) for 4 h, changing the buffer once after 2 h, and stored on ice.

To polymerize actin and myosin and assemble actomyosin networks, $0.23\ \mu\text{M}$ myosin II dimers and $11.6\ \mu\text{M}$ actin monomers (at a molar ratio of 1:10 of Alexa-568-labeled and unlabeled actin monomers) are mixed and incubated in F-buffer (10 mM Imidazole pH 7.0, 50 mM KCl, 1 mM MgCl_2 , 1 mM



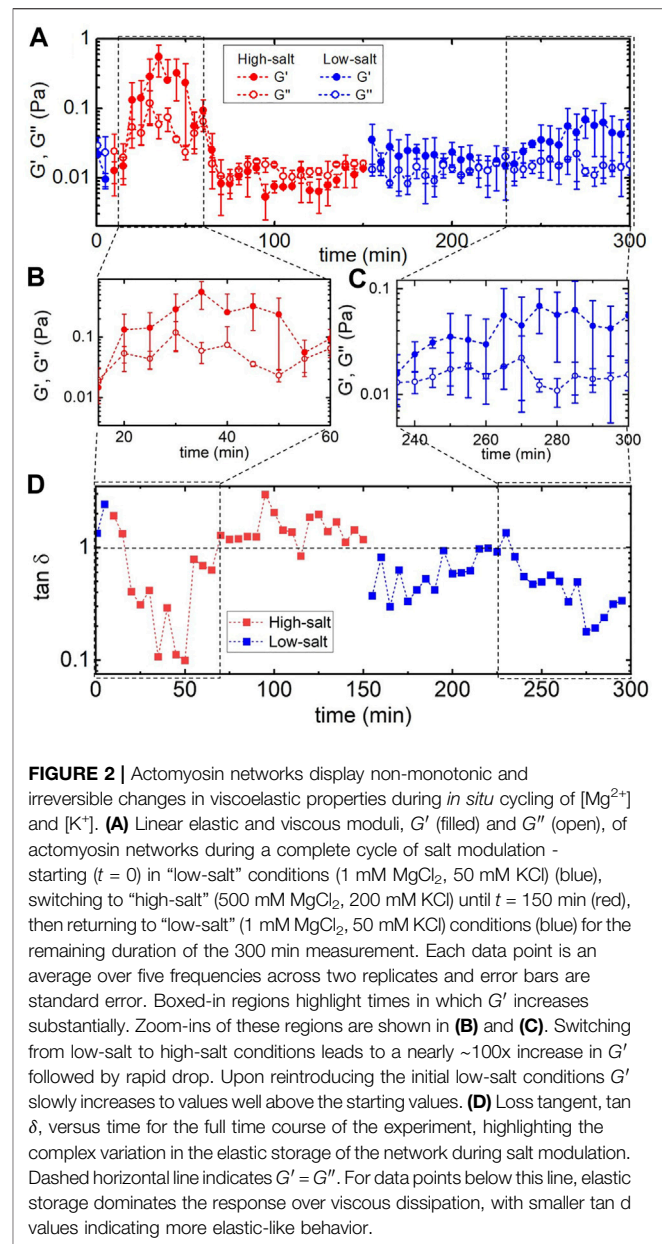
EGTA, 0.2 mM ATP) for 1 h at room temperature. For reference, the nominal mesh size of an actin network with concentration $c_a = 0.5\ \text{mg/ml}$ ($11.6\ \mu\text{M}$) is $\xi \approx 0.3/\sqrt{c_a} \approx 0.42\ \mu\text{m}$ [45]. Note that the initial Mg^{2+} and K^+ concentrations are 1 and 50 mM, respectively, and the ATP level is low enough to prevent noticeable myosin II ATPase activity. A trace amount of Alexa Fluor 488-BSA-coated polystyrene microspheres (Polysciences Inc.), with radius $a = 2.25\ \mu\text{m}$, is added for microrheology measurements. The microsphere diameter was chosen to be ~ 5 times larger than the network mesh size, such that our microrheology measurements described below are reporting the properties of the full network [46–48].

Microfluidics: The microfluidic device shown in Figure 1 is assembled as previously described [33,49,50]. Briefly, a coverslip (no. 0, $22 \times 22\ \text{mm}$) and glass slide are washed thoroughly with acetone, isopropanol, and deionized water (DI), then plasma

cleaned. A parafilm spacer is placed between the slip and slide and the resulting chamber is fused together using a soldering iron. To form two semipermeable membranes in the chamber, a 50:1 mixture of poly (ethylene glycol) diacrylate (PEG-DA) and a photoinitiator (2-hydroxy-2-methylpropiophenone) diluted to 20% (v/v) in DI, are flowed into the chamber. The chamber is then exposed to UV through a custom photomask to form two cross-linked PEG-DA membranes, and flushed with DI to remove the PEG-DA solution. This process results in a central chamber for holding the sample separated by semipermeable membranes from two flanking channels that enable buffer exchange *via* diffusion (**Figure 1A**).

For experiments, the actomyosin solution is pipetted into the central chamber, and the flanking buffer channels are filled with F-buffer. Buffer channels are then connected to capillary tubes at both ends. Both tubes from one end are connected to Tygon tubing I, which is connected to a syringe pump, while the tubes at the other end are connected to two separate Tygon tubing II which are inserted into a buffer reservoir to enable buffer exchange. All channels are then sealed with epoxy. Using the syringe pump, the existing buffer is pulled from the buffer channels at a flow rate of 5 $\mu\text{l}/\text{min}$ as new buffer from the reservoir is pulled in, thereby enabling diffusion-controlled buffer exchange into the central chamber. To vary the buffer conditions between “low-salt” (1 mM MgCl_2 and 50 mM KCl) and “high-salt” (500 mM MgCl_2 and 200 mM KCl), the F-buffer in the reservoir is replaced with F-buffer containing the “high” concentrations of MgCl_2 and KCl at the beginning of the 300 min experiment (**Figure 1B**). After 150 min, the buffer in the reservoir is replaced with the initial “low-salt” F-buffer. Complete buffer exchange in each cycle is achieved in ~ 10 min. Note that the concentrations of all other buffer components remain constant throughout the experiment.

Microrheology: The optical trap used in microrheology measurements was built by outfitting an Olympus IX71 fluorescence microscope with a 1064 nm ND:YAG fiber laser (Manlight) focused with a 60x 1.4 NA objective, as previously thoroughly described [51–53]. The trap stiffness was calibrated *via* Stokes drag in water [54,55] and passive equipartition methods [56], as previously described and validated [52,53]. For each measurement, a probe embedded in the sample is trapped and oscillated sinusoidally relative to the sample at an amplitude of $x_0 = 1.0 \mu\text{m}$ at five frequencies from $\omega = 0.5$ to 107 rad/s by using a piezoelectric nanopositioning stage (Mad City Laboratories) to oscillate the sample while keeping the trap fixed. A position-sensing detector (First Sensor) measures the laser deflection, which is proportional to the force F exerted on the probe by the surrounding network. We analyze the stage position and laser deflection for each trial to ensure that the stage completes full amplitude oscillations and the bead remains trapped for the duration of the measurement. The stage position and force data are both fit to sine curves using the least-squares method, from which the frequency-dependent elastic modulus G' and viscous modulus G'' are computed *via* $G' = |F_o| \cos(\Delta\phi)/6\pi a |X_o|$ and $G'' = |F_o| \sin(\Delta\phi)/6\pi a |X_o|$, where F_o and $\Delta\phi$ are the amplitude of measured force F and the



phase shift between the force and the stage oscillations. Measurements are performed every 5 min over the course of 300 min where $t = 0$ is immediately before exchange from low-to high-salt buffer is initiated, and $t = 150$ min is immediately before exchange from high-salt back to low-salt buffer begins. G' and G'' data shown in **Figure 2** are averaged over all frequencies for two replicates and error bars are the standard error of these values. As shown in **Supplementary Figure S1**, while there is modest frequency dependence of G' and G'' , this dependence does not depend on the measurement time, so averaging over frequency does not impact the time-dependence shown in **Figure 2**. Further, due to the dynamic nature of the network, there is inherent noise in the measurement due to network fluctuations, such that

averaging over a range of frequencies results in more robust measured trends.

Microscopy: To gain insight into the salt-mediated structural reorganization of actomyosin networks during exchanging between low-salt and high-salt conditions, the same buffer exchange program described above is performed while imaging the Alexa-568-labeled actin comprising the actomyosin networks using a Nikon A1R laser scanning confocal microscope with 60x 1.4 NA objective and 561 nm laser line. Single 512×512 pixel images are collected every minute for a total of 300 min. To quantify the network structure at various time-points during the experiment, a custom-written python script was used to perform spatial image autocorrelation (SIA) analysis on each image [57]. SIA measures the correlation $g(r)$ in intensity $I(r)$ of two pixels in an image as a function of separation distance r . We generate each autocorrelation curve by taking the fast Fourier transform of an image, multiplying by its complex conjugate, applying an inverse Fourier transform, and then normalizing by the intensity squared: $g(r) = F^{-1}(|F(I(r))|^2)/[I(r)]^2$ where F and F^{-1} represent fast Fourier and inverse Fourier transforms, respectively. The corresponding correlation length ξ is obtained by curve-fitting autocorrelation curves to $g(r) = g_0 \exp(-r/\xi)$. This approach is based on previous studies that have applied SIA to confocal images of cytoskeleton networks to determine correlation lengthscales [58,59]. Because many of the curves exhibit non-exponential tails at large distances due to flat-field noise, as in these prior studies, we restrict curve-fitting to $g(r \leq 2 \mu\text{m})$.

3 RESULTS AND DISCUSSION

To determine the effect of combined increases in Mg^{2+} and K^+ on the mechanics and structure of actomyosin networks, we use microfluidic perfusion chambers to modulate the counterion concentration without inducing flow or disrupting the network. Importantly, we keep the ATP concentration low such that the enzymatic activity of the myosin motors is suppressed [26]. We form networks in the standard “low-salt” buffer (containing 1 mM MgCl_2 and 50 mM KCl) in the microfluidic chamber. At the start of our measurements (either microrheology or confocal imaging), we immediately switch to the “high-salt” buffer (with 500 mM MgCl_2 and 200 mM KCl), and after 150 min we exchange the buffer again to return to the initial “low-salt” buffer. The low-salt conditions have been shown to result in homogeneous entangled networks of individual actin filaments [7,13,14,18–20,55,60] and the formation of myosin-II minifilaments that crosslink actin [43,61]. Mg^{2+} concentrations above ~ 20 mM have been shown to induce substantial bundling of actin filaments [33,34], while $[\text{K}^+]$ greater than ~ 150 mM depolymerizes myosin-II minifilaments [43,44].

We perform time-resolved optical tweezers microrheology measurements during the course of the 300-min cycle of salt modulation to determine how the mechanical properties of the network vary in response to changing salt concentrations. We complement these measurements with corresponding confocal

imaging experiments to link the changing viscoelastic properties of the network to the structure.

Figure 2 displays the results of our microrheology measurements, which reveal non-monotonic and irreversible changes to the viscoelastic moduli of actomyosin networks upon introduction of high-salt conditions. Specifically, G' and G'' both increase as high-salt buffer is introduced, reaching a maximum at ~ 35 min, before dropping to values below their starting values, which remain constant for the duration of the high-salt period. Upon returning to low-salt conditions at 150 min there is modest increase in the elastic modulus that remains constant until ~ 240 min at which point G' steadily increases for ~ 30 min before reaching a steady value that is nearly an order of magnitude larger than the value at $t = 0$. Both periods of increased G' values (in high-salt and low-salt conditions) display elastic behavior with G' significantly larger than G'' , as shown in **Figures 2B,C**. To better quantify the time-varying elastic storage of the network we compute the loss tangent, $\tan \delta = G''/G'$, which is a measure of the viscous dissipation in the system (**Figure 2D**). $\tan \delta > 1$ indicates largely viscous behavior while $\tan \delta < 1$ indicates elastic-like behavior with lower values indicating increased elastic storage. As shown, the elasticity increases dramatically at the beginning of the high-salt phase and then abruptly drops to a viscous-dominated regime. Substantial elasticity is not recovered until near the end of the subsequent low-salt phase.

Two features of the described time-varying mechanical properties that are surprising and notable are: 1) the abrupt drop in $\tan \delta$ after the initial increase, and 2) the increase in $\tan \delta$ at the end of the low-salt phase. To understand feature (1), we recall that high Mg^{2+} concentrations induce actin bundling and crosslinking *via* counterion crossbridges [26,27,31], which we expect to result in increased elasticity [50], as we see in the first ~ 30 min of the experiment. However, the unexpected subsequent drop to a viscous-dominated regime suggests disruption of myosin-crosslinks, as seen in previous studies on steady-state actomyosin networks [25–27]. We postulate that this effect is due to the high $[\text{K}^+]$ conditions depolymerizing myosin II minifilaments, as described in the Introduction [43,50], and thus destroying the crosslinks they form between actin filaments. In the following section, we shed further light on the structural evolution that competing effects of actin bundling and myosin minifilament disassembly give rise to. Feature (2) is counterintuitive as one would expect that returning the system to its initial buffer conditions would cause the system to return to a state similar to its initial state. Namely, we would expect actin filaments to de-bundle and myosin II minifilaments to reform and re-connect actin filaments, such that G' and G'' at $t = 0$ and $t = 300$ min would be similar. Instead we find that the network exhibits substantially more elasticity at the end of the experiment than at the beginning - suggestive of more bundling or connectivity. This effect implies that there are irreversible processes at play and that the network is encoding information about its previous state (i.e., mechano-memory). We investigate this phenomenon further below.

We note that the error bars shown in **Figure 2**, which represent the standard error (SE), are indeed larger than is typical in steady-state microrheology measurements [34], with

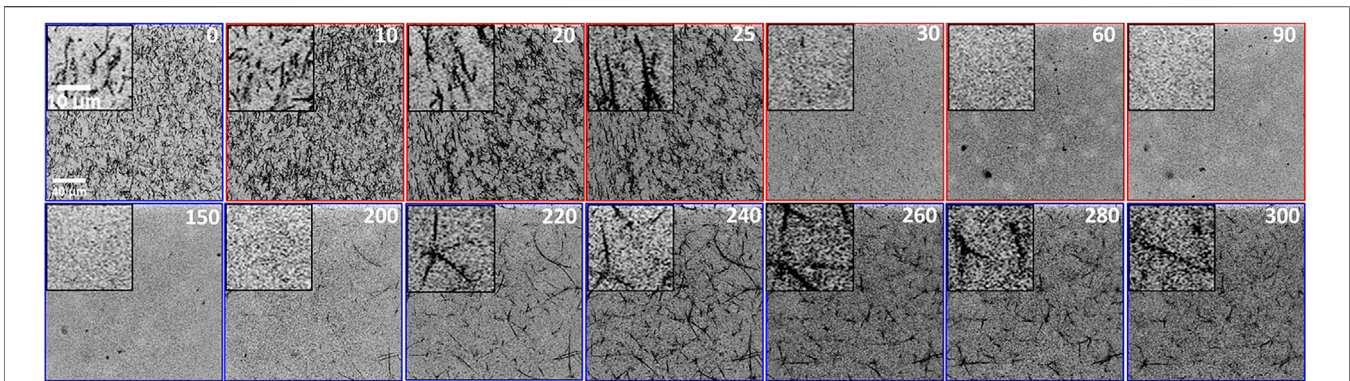


FIGURE 3 | Laser scanning confocal microscopy images of fluorescent-labeled actin filaments comprising actomyosin networks subject to *in situ* cycling of $[Mg^{2+}]$ and $[K^+]$. The buffer exchange program is identical to that done for microrheology measurements. Times are listed in minutes in the top right corner of each image. Scale bars shown for $t = 0$ apply to all images and are $40 \mu\text{m}$ for main images and $10 \mu\text{m}$ for the zoomed-in insets. Colors around each image indicate the buffer conditions as in **Figure 2** [blue = low-salt (1 mM $MgCl_2$, 50 mM KCl), red = high-salt (500 mM $MgCl_2$, 200 mM KCl)]. At $t = 0$ the network is homogeneous and comprised of thin fibers. Switching to “high-salt” leads to thickening (i.e., bundling) of fibers ($t = 10, 20,$ and 30) followed by network destruction ($t = 60, 90,$ and 150). Re-introducing “low-salt” buffer leads to slow re-emergence of networks that are substantially more bundled than the initial low-salt network ($t = 200, 240, 280,$ and 300). Each 512×512 inverted greyscale image is captured using an A1R laser scanning fluorescence confocal microscope with 60×1.4 NA objective and 561 nm laser line.

corresponding percent error ($PE = SE/mean$) values that average to $\langle PE \rangle = 31\%$ and 38% for G' and G'' , respectively. This spread is a result of: 1) averaging over all frequencies, as there is a modest frequency dependence of G' and G'' (which does not depend on time, see **Supplementary Figure S1**); and 2) the dynamic nature of the system (i.e., its rheological and structural properties are changing over time), such that there are larger fluctuations than for a steady-state system. As such, to demonstrate the statistical significance of our measured trends, we compare $\langle PE \rangle$ to the percent variation in $G'(t)$ and $G''(t)$ over the course of the experimental time t . Specifically, we average over all G' and G'' values over the course of the experiment ($\langle G \rangle_t$), and determine the corresponding percent error (PE_t), which has values of $PE_t = 111\%$ and 64% for G' and G'' respectively, both significantly larger than the corresponding $\langle PE \rangle$ values.

To shed light on the structural changes that give rise to the salt-mediated variation in the viscoelastic response of the network, we turn to our confocal imaging experiments performed under the exact conditions as the microrheology measurements (**Figure 2**, **Supplementary Movie S1**). **Figure 3** shows images of the fluorescent-labeled actin filaments comprising the network at different time points during the salt modulation. The top row shows the structural evolution in high-salt conditions ($t < 150$ min) while the bottom row shows the low-salt phase ($t > 150$ min). As shown, the network formed under low-salt conditions ($t = 0$ min) is homogeneous and comprised of thin fibers. The minimal thermal noise in the images indicates substantial crosslinking *via* myosin minifilaments [26,50]. However, upon introduction of high-salt buffer, the fibers become darker and thicker, indicating bundling. The mesh size appears to increase accordingly as the network transitions to one composed of fewer, thicker bundles. Surprisingly, after ~ 30 min, the network rapidly dissolves, with no signs of fibers for the remaining duration of the high-salt period (until $t = 150$ min). Fragments of disconnected fibers would appear as thermal noise

so the absence of any clear structure suggests that the bundles are no longer connected and are thus rapidly diffusing. This destruction is likely the result of the crosslinking myosin II minifilaments depolymerizing due to the increased $[K^+]$, thereby disrupting actin network connectivity. Further, reintroducing the initial low-salt buffer leads to the re-emergence of stable actin networks. However, these networks are markedly different than the initial network, despite the fact that the buffer conditions are identical. Specifically, the reformed networks are comprised of much thicker and apparently stiffer (i.e., less bent by thermal fluctuations) fibers that are more sparsely connected. This irreversibility suggests that while myosin minifilaments can reform as $[K^+]$ is lowered, salt-induced actin bundling is not reversible, likely due to entropic depletion interactions [44,50,62].

We note that in **Figure 3**, the network appears to reach maximum bundling at ~ 25 min (see **Supplementary Movie S1**) rather than at ~ 30 – 35 min, where we measure a minimum in $\tan \delta$ in **Figure 2**. Nevertheless, we maintain that maximal bundling coincides with maximal G' values (and minima in $\tan \delta$), and that this ~ 5 – 10 min difference, which equates to $\leq 3\%$ of the total measurement time, is due to sample-to-sample variation. Specifically, confocal experiments were performed on different samples than microrheology experiments, so we expect there to be slight differences in the time at which peak bundling and network elasticity occur. These variations are also evident in the different microrheology trials we conducted and add to the spread in the microrheology data shown in **Figure 2**.

To quantify the structural changes depicted in **Figure 3**, we compute the spatial image autocorrelation function $g(r)$ as a function of distance r between pixels for each image shown in **Figures 4A,B**. Faster decay of $g(r)$ with r indicates smaller network features and a higher initial value indicates brighter features and higher signal-to-noise (resulting from filament bundling or clustering). As shown, autocorrelation curves increase in magnitude and decay more slowly as t increases

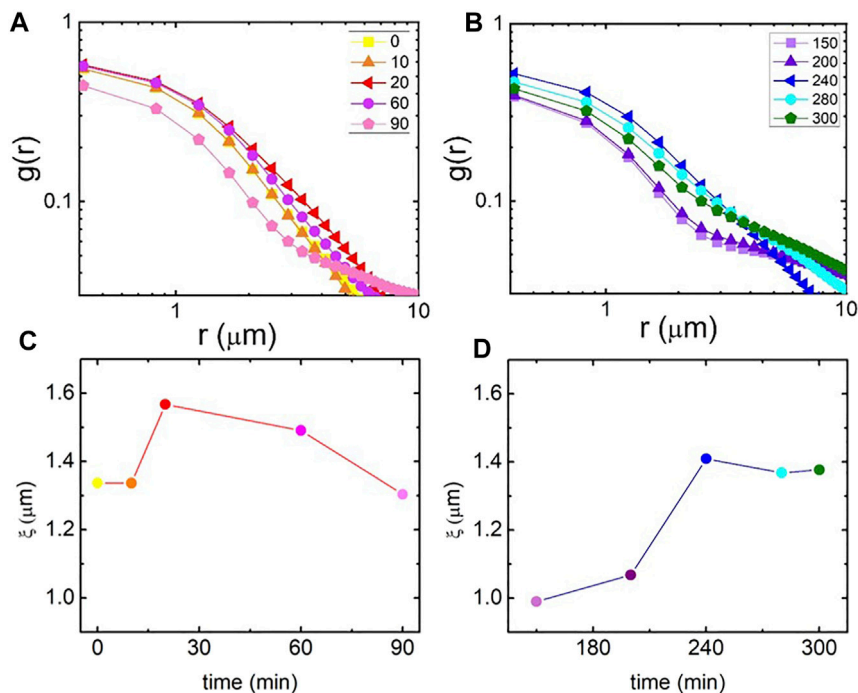


FIGURE 4 | Spatial image autocorrelation analysis quantifies the salt-mediated structural changes to actomyosin networks that give rise to the time-varying viscoelastic properties. **(A, B)** Spatial image autocorrelation functions $g(r)$ versus distance r computed from confocal images shown in **Figure 3**. Plots are divided into “high-salt” **(A)** and “low-salt” **(B)** conditions with the experimental time (in min) of each image listed in the legend. **(C, D)** Structural correlation lengths ξ determined from fitting each $g(r)$ shown in **(A)** and **(B)** to an exponential decay function $g(r) \sim e^{-r/\xi}$. ξ , which indicates the average size of structural features, shows bundling (increasing ξ) and subsequent destruction (drop in ξ) during the high-salt period **(C)**, followed by re-assembly into highly-bundled networks during the low-salt period **(D)**, increase in ξ to value larger than $t = 0$ value.

from 0 to ~ 30 min (the time period at which we observe substantial bundling), after which $g(0)$ is reduced and $g(r)$ decays more quickly until ~ 200 min (the time over which the network is destroyed), at which point $g(0)$ increases once again and the decay becomes more broad as the network reforms.

Because all curves exhibit exponential decay for distances up to $\sim 2 \mu\text{m}$, we fit this portion of each curve to $g(r) = g_0 \exp(-r/\xi)$ to extract a characteristic correlation length ξ for the network as a function of time. This correlation length, which is proportional to the mesh size for an isotropic polymer network, displays noticeable changes that track with the rheological changes we present in **Figure 2**. Specifically, ξ displays a non-monotonic dependence on time during the high-salt phase, peaking at a similar time at which the loss tangent exhibits a minimum, indicating that the highly bundled network retains the most elastic storage, in line with previous experiments [34]. During the low-salt re-introduction ξ steadily rises starting at ~ 200 min, when we observe network reformation and a decrease in $\tan \delta$. ξ continues to increase until ~ 240 min when the network appears to stabilize and $\tan \delta$ reaches a new minimum. As ξ is a measure of the average size of the features of the network, this lengthscale could be reporting the mesh size or the bundle size. However, because the formation of bundles leads to larger mesh sizes, as the network becomes composed of fewer, but more rigid, fibers, the bundling lengthscale and mesh size should scale together.

Further, the time dependence of both of these feature sizes should track with $\tan \delta$, as we see in **Figures 2, 4**.

We note that these findings differ from those previously reported for entangled composites of DNA and actin in which actin bundling led to a decrease in network elasticity [63]. In this previous work, the loss of elasticity was due to bundling destroying the percolation of the actin network. As the actin filaments bundled together, the mesh size grew (as in our system), eventually surpassing a critical point at which percolation was destroyed and thus the network was no longer predominantly elastic. In our current work, we do not reach this critical point, as evidenced by the confocal images that show that bundles remain connected. These connections are likely further facilitated by the myosin crosslinkers which were not present in the DNA-actin composites.

Finally, it is informative to contrast our results with those expected in the absence of either $[\text{Mg}^{2+}]$ or $[\text{K}^+]$ modulation. Previous studies [33] examined the bulk conformational changes of actin networks subject to increasing and decreasing $[\text{Mg}^{2+}]$. These experiments showed that actin networks bundle and contract as $[\text{Mg}^{2+}]$ increases, as we see here, but actually continue to bundle when $[\text{Mg}^{2+}]$ is subsequently lowered, albeit at a slower rate. There is no observed network dissolution in these studies. As such, we expect that under Mg^{2+} modulation only, we would observe continued bundling over the course of the experiment; however, upon cycling back to

low $[Mg^{2+}]$ conditions, the network would slow bundling significantly but remain in a bundled state rather than returning to its starting structure (a network of individual filaments). Based on the reported effect of $[KCl]$ on myosin polymerization and stability [64], as we discuss above, as well as the evidence that monovalent salt does not effectively bundle actin filaments [64,65], we expect that networks subject to $[K^+]$ modulation only would show minimal bundling, and would instead exhibit elastic weakening as $[K^+]$ increases due to the crosslinking myosin minifilaments falling apart. Upon decreasing $[K^+]$ again the network would reconnect and rigidify, likely returning to a crosslinked state similar to its initial state.

4 CONCLUSION

Here, we elucidate the effects of simultaneous cycling of Mg^{2+} and K^+ concentrations on the mechanics and structure of actin networks crosslinked *via* myosin II minifilaments. We find that while increasing $[Mg^{2+}]$ serves to bundle actin filaments, increasing network strength and elasticity, increasing $[K^+]$ destabilizes crosslinking myosin II minifilaments, thereby compromising the connectivity and integrity of the network.

Specifically, we couple time-resolved optical tweezers microrheology and confocal fluorescence imaging with microfluidic perfusion chambers to characterize the time-varying viscoelastic and structural properties of actomyosin networks as we cycle the buffer conditions from low-salt (1 mM $MgCl_2$ and 50 mM KCl) to high-salt (500 mM $MgCl_2$ and 200 mM KCl), then back to low-salt. Our results reveal a surprising non-monotonic time-dependence of the network elasticity under high-salt conditions, which mirrors the time course of actin bundling and subsequent network destruction. Namely, we observe a dramatic rise in the elastic modulus, coupled to increased actin bundling, followed by an abrupt drop to a viscous-dominated regime and apparent destruction of a connected network. We postulate that this complex time-dependence arises from the increased $[Mg^{2+}]$ driving actin bundling *via* charge-screening, followed by slower $[K^+]$ -triggered depolymerization of myosin II minifilaments that disconnect and disrupt the network of bundles. Upon lowering $[Mg^{2+}]$ and $[K^+]$ back to their initial concentrations, a connected network slowly re-emerges but with features that are distinct from the initial networks formed in the same ionic conditions. Namely, the network exhibits increased elasticity and more bundled features, suggesting that while connectivity can be restored as myosin II minifilaments re-polymerize, actin bundling cannot be as easily reversed.

Our robust experimental approach can be applied to wide-ranging soft and active materials to explore how varying

environmental conditions alter the mechanics and structure of the system in real-time. Further, our results shed important light on the various mechanisms that the cytoskeleton can use to alter its mechanical and structural features. More generally, our results demonstrate that the mechanical response of biopolymer networks can encode information regarding their previous state, which may be exploited in the design of next-generation biosensors, memory storage devices, and other smart materials applications. In future work, we will explore how varying the concentrations of actin and myosin, as well as the types and concentrations of salts, can be used to tune the mechanical and structural response of cytoskeleton networks.

DATA AVAILABILITY STATEMENT

The original contributions presented in the study are included in the article/**Supplementary Material**, further inquiries can be directed to the corresponding author.

AUTHOR CONTRIBUTIONS

BG conducted experiments, analyzed and interpreted data, and wrote the manuscript. RR-A designed and guided experiments, analyzed and interpreted data, and wrote the manuscript. MR, MD, and JR advised on experimental design and results.

FUNDING

This research was funded by an NSF CAREER Award (No. 1255446) to RR-A and a W. M. Keck Foundation Research Grant to RR-A, MR, MD, and JR.

ACKNOWLEDGMENTS

We thank Prof David Kovar and Caitlin Anderson for providing us with myosin II along with corresponding handling protocols and guidance. We thank Shea Ricketts for assistance with microfluidic device assembly and confocal imaging.

SUPPLEMENTARY MATERIAL

The Supplementary Material for this article can be found online at: <https://www.frontiersin.org/articles/10.3389/fphy.2021.760340/full#supplementary-material>

REFERENCES

1. Insall R Actin in 2021. *Curr Biol* (2021) 31:R496–R498. doi:10.1016/j.cub.2021.04.013
2. Gardel ML, Kasza KE, Brangwynne CP, Liu J, Weitz DA Chapter 19 Mechanical Response of Cytoskeletal Networks. *Methods Cel Biol* (2008) 89:487–519. doi:10.1016/s0091-679x(08)00619-5
3. Blanchoin L, Boujemaa-Paterski R, Sykes C, Plastino J Actin Dynamics, Architecture, and Mechanics in Cell Motility. *Physiol Rev* (2014) 94: 235–63. doi:10.1152/physrev.00018.2013
4. Svitkina T The Actin Cytoskeleton and Actin-Based Motility. *Cold Spring Harb Perspect Biol* (2018) 10:a018267. doi:10.1101/cshperspect.a018267
5. Cooper GM Structure and Organization of Actin Filaments. In: *The Cell: A Molecular Approach 2* (2000).

6. Bausch AR, Kroy K A Bottom-Up Approach to Cell Mechanics. *Nat Phys* (2006) 2:231–8. doi:10.1038/nphys260
7. Schmoller KM, Lieleg O, Bausch AR Structural and Viscoelastic Properties of Actin/filamin Networks: Cross-Linked versus Bundled Networks. *Biophysical J* (2009) 97:83–9. doi:10.1016/j.bpj.2009.04.040
8. Castaneda N, Park J, Kang EH Regulation of Actin Bundle Mechanics and Structure by Intracellular Environmental Factors. *Front Phys* (2021) 9:227. doi:10.3389/fphy.2021.675885
9. Lieleg O, Schmoller KM, Cyron CJ, Luan Y, Wall WA, Bausch AR Structural Polymorphism in Heterogeneous Cytoskeletal Networks. *Soft Matter* (2009) 5: 1796–803. doi:10.1039/b814555p
10. Tharmann R, Claessens MM, Bausch AR. Viscoelasticity of Isotropically Cross-Linked Actin Networks. *Phys Rev Lett* (2007) 98:088103. doi:10.1103/PhysRevLett.98.088103
11. Shin JH, Mahadevan L, So PT, Matsudaira P Bending Stiffness of a Crystalline Actin Bundle. *J Mol Biol* (2004) 337:255–61. doi:10.1016/j.jmb.2004.01.028
12. Lieleg O, Claessens MM, Heussinger C, Frey E, Bausch AR. Mechanics of Bundled Semiflexible Polymer Networks. *Phys Rev Lett* (2007) 99:088102. doi:10.1103/PhysRevLett.99.088102
13. Stricker J, Falzone T, Gardel ML Mechanics of the F-Actin Cytoskeleton. *J Biomech* (2010) 43:9–14. doi:10.1016/j.jbiomech.2009.09.003
14. Janmey PA, Hvidt S, Käs J, Lerche D, Maggs A, Sackmann E, et al. The Mechanical Properties of Actin Gels. Elastic Modulus and Filament Motions. *J Biol Chem* (1994) 269:32503–13. doi:10.1016/s0021-9258(18)31663-6
15. Käs J, Strey H, Tang JX, Finger D, Ezzell R, Sackmann E, et al. F-actin, a Model Polymer for Semiflexible Chains in Dilute, Semidilute, and Liquid Crystalline Solutions. *Biophysical J* (1996) 70:609–25. doi:10.1016/s0006-3495(96)79630-3
16. Koenderink GH, Atakhorrami M, MacKintosh FC, Schmidt CF High-frequency Stress Relaxation in Semiflexible Polymer Solutions and Networks. *Phys Rev Lett* (2006) 96:138307. doi:10.1103/physrevlett.96.138307
17. Liu J, Koenderink GH, Kasza KE, MacKintosh FC, Weitz DA Visualizing the Strain Field in Semiflexible Polymer Networks: Strain Fluctuations and Nonlinear Rheology of off-Actin Gels. *Phys Rev Lett* (2007) 98:198304. doi:10.1103/physrevlett.98.198304
18. Broeders CP, Kasza KE, Jawerth LM, Münster S, Weitz DA, MacKintosh FC Measurement of Nonlinear Rheology of Cross-Linked Biopolymer Gels. *Soft Matter* (2010) 6:4120–7. doi:10.1039/c0sm00285b
19. Claessens MMAE, Bathe M, Frey E, Bausch AR Actin-binding Proteins Sensitive Mediate F-Actin Bundle Stiffness. *Nat Mater* (2006) 5:748–53. doi:10.1038/nmat1718
20. Lieleg O, Kayser J, Brambilla G, Cipelletti L, Bausch AR Slow Dynamics and Internal Stress Relaxation in Bundled Cytoskeletal Networks. *Nat Mater* (2011) 10:236–42. doi:10.1038/nmat2939
21. Ideses Y, Sonn-Segev A, Roichman Y, Bernheim-Groswasser A Myosin II Does it All: Assembly, Remodeling, and Disassembly of Actin Networks Are Governed by Myosin II Activity. *Soft Matter* (2013) 9:7127–37. doi:10.1039/c3sm50309g
22. Betapudi V Life without Double-Headed Non-muscle Myosin II Motor Proteins. *Front Chem* (2014) 2:45. doi:10.3389/fchem.2014.00045
23. Soares e Silva MMS, Stuhmann B, Betz T, Koenderink GH Time-resolved Microrheology of Actively Remodeling Actomyosin Networks. *New J Phys* (2014) 16:075010. doi:10.1088/1367-2630/16/7/075010
24. Laevsky G, Knecht DA Cross-linking of Actin Filaments by Myosin II Is a Major Contributor to Cortical Integrity and Cell Motility in Restrictive Environments. *J Cell Sci* (2003) 116:3761–70. doi:10.1242/jcs.00684
25. Wachsstock DH, Schwarz WH, Pollard TD Cross-linker Dynamics Determine the Mechanical Properties of Actin Gels. *Biophysical J* (1994) 66:801–9. doi:10.1016/s0006-3495(94)80856-2
26. Humphrey D, Duggan C, Saha D, Smith D, Käs J Active Fluidization of Polymer Networks through Molecular Motors. *Nature* (2002) 416:413–6. doi:10.1038/416413a
27. Koenderink GH, Dogic Z, Nakamura F, Bendix PM, MacKintosh FC, Hartwig JH, et al. An Active Biopolymer Network Controlled by Molecular Motors. *Proc Natl Acad Sci* (2009) 106:15192–7. doi:10.1073/pnas.0903974106
28. Reichl EM, Ren Y, Morphew MK, Delannoy M, Effler JC, Girard KD, et al. Interactions between Myosin and Actin Crosslinkers Control Cytokinesis Contractility Dynamics and Mechanics. *Curr Biol* (2008) 18:471–80. doi:10.1016/j.cub.2008.02.056
29. Martens JC, Radmacher M Softening of the Actin Cytoskeleton by Inhibition of Myosin II. *Pflugers Arch - Eur J Physiol* (2008) 456:95–100. doi:10.1007/s00424-007-0419-8
30. Rauzi M, Lenne P-F Cortical Forces in Cell Shape Changes and Tissue Morphogenesis. In: M Labouesse, editor. *Forces and Tension in Development*, 95. Academic Press Current Topics in Developmental Biology (2011). p. 93–144. 93 – 144. doi:10.1016/B978-0-12-385065-2.00004-9
31. Mizuno D, Tardin C, Schmidt CF, MacKintosh FC Nonequilibrium Mechanics of Active Cytoskeletal Networks. *Science* (2007) 315:370–3. doi:10.1126/science.1134404
32. Huxley HE Fifty Years of Muscle and the Sliding Filament Hypothesis. *Eur J Biochem* (2004) 271:1403–15. doi:10.1111/j.1432-1033.2004.04044.x
33. Ricketts SN, Khanal P, Rust MJ, Das M, Ross JL, Robertson-Anderson RM Triggering Cation-Induced Contraction of Cytoskeleton Networks via Microfluidics. *Front Phys* (2020) 8:596699. doi:10.3389/fphy.2020.596699
34. Gurmessa B, Francis M, Rust MJ, Das M, Ross JL, Robertson-Anderson RM Counterion Crossbridges Enable Robust Multiscale Elasticity in Actin Networks. *Phys Rev Res* (2019) 1:013016. doi:10.1103/physrevresearch.1.013016
35. MacKintosh FC, Schmidt CF Active Cellular Materials. *Curr Opin Cell Biol* (2010) 22:29–35. doi:10.1016/j.ceb.2010.01.002
36. Wen Q, Janmey PA Polymer Physics of the Cytoskeleton. *Curr Opin Solid State Mater Sci* (2011) 15:177–82. doi:10.1016/j.cossms.2011.05.002
37. Cooper GM, Ganem D The Cell: A Molecular Approach. *Nat Med* (1997) 3: 1042.
38. Deshpande S, Pfohl T Real-time Dynamics of Emerging Actin Networks in Cell-Mimicking Compartments. *PloS one* (2015) 10:e0116521. doi:10.1371/journal.pone.0116521
39. Huber F, Strehle D, Käs J Counterion-induced Formation of Regular Actin Bundle Networks. *Soft Matter* (2012) 8:931–6. doi:10.1039/c1sm06019h
40. Huber F, Strehle D, Schnauß J, Käs J Formation of Regularly Spaced Networks as a General Feature of Actin Bundle Condensation by Entropic Forces. *New J Phys* (2015) 17:043029. doi:10.1088/1367-2630/17/4/043029
41. Castaneda N, Zheng T, Rivera-Jacquez HJ, Lee H-J, Hyun J, Balaeff A, et al. Cations Modulate Actin Bundle Mechanics, Assembly Dynamics, and Structure. *J Phys Chem B* (2018) 122:3826–35. doi:10.1021/acs.jpcc.8b00663
42. Strehle D, Schnauß J, Heussinger C, Alvarado J, Bathe M, Käs J, et al. Transiently Crosslinked F-Actin Bundles. *Eur Biophys J* (2011) 40:93–101. doi:10.1007/s00249-010-0621-z
43. Kaminer B, Bell AL Myosin Filamentogenesis: Effects of Ph and Ionic Concentration. *J Mol Biol* (1966) 20:391–401. doi:10.1016/0022-2836(66)90070-2
44. Matsuda K, Kobayashi T, Sugawa M, Koiso Y, Toyoshima YY, Yajima J Myosin-driven Fragmentation of Actin Filaments Triggers Contraction of a Disordered Actin Network. *bioRxiv* (2018) 332684.
45. Isambert H, Maggs AC Dynamics and Rheology of Actin Solutions. *Macromolecules* (1996) 29:1036–40. doi:10.1021/ma946418x
46. Weigand WJ, Messmore A, Tu J, Morales-Sanz A, Blair DL, Deheyn DD, et al. Active Microrheology Determines Scale-dependent Mechanical Properties of Chaetopterus Mucus. *PloS one* (2017) 12:e0176732. doi:10.1371/journal.pone.0176732
47. Chapman CD, Lee K, Henze D, Smith DE, Robertson-Anderson RM Onset of Non-continuum Effects in Microrheology of Entangled Polymer Solutions. *Macromolecules* (2014) 47:1181–6. doi:10.1021/ma401615m
48. Francis ML, Ricketts SN, Farhadi L, Rust MJ, Das M, Ross JL, et al. Non-monotonic Dependence of Stiffness on Actin Crosslinking in Cytoskeleton Composites. *Soft Matter* (2019) 15:9056–65. doi:10.1039/c9sm01550g
49. Park C-Y, Jacobson DR, Nguyen DT, Willardson S, Saleh OA A Thin Permeable-Membrane Device for Single-Molecule Manipulation. *Rev Scientific Instr* (2016) 87:014301. doi:10.1063/1.4939197
50. Gurmessa BJ, Bitten N, Nguyen DT, Saleh OA, Ross JL, Das M, et al. Triggered Disassembly and Reassembly of Actin Networks Induces Rigidity Phase Transitions. *Soft matter* (2019) 15:1335–44. doi:10.1039/c8sm01912f
51. Robertson-Anderson RM *Optical Tweezers Microrheology: From the Basics to Advanced Techniques and Applications* (2018). Dataset.

52. Gurmessa B, Ricketts S, Robertson-Anderson RM Nonlinear Actin Deformations lead to Network Stiffening, Yielding, and Nonuniform Stress Propagation. *Biophysical J* (2017) 113(7):1540–50. doi:10.1016/j.bpj.2017.01.012
53. Falzone TT, Blair S, Robertson-Anderson RM Entangled F-Actin Displays a Unique Crossover to Microscale Nonlinearity Dominated by Entanglement Segment Dynamics. *Soft matter* (2015) 11:4418–23. doi:10.1039/c5sm00155b
54. Falzone TT, Robertson-Anderson RM Active Entanglement-Tracking Microrheology Directly Couples Macromolecular Deformations to Nonlinear Microscale Force Response of Entangled Actin. *ACS Macro Lett* (2015) 4:1194–9. doi:10.1021/acsmacrolett.5b00673
55. Gurmessa B, Fitzpatrick R, Falzone TT, Robertson-Anderson RM Entanglement Density Tunes Microscale Nonlinear Response of Entangled Actin. *Macromolecules* (2016) 49:3948–55. doi:10.1021/acs.macromol.5b02802
56. Brau RR, Ferrer JM, Lee H, Castro CE, Tam BK, Tarsa PB, et al. Passive and Active Microrheology with Optical Tweezers. *J Opt A: Pure Appl Opt* (2007) 9: S103–S112. doi:10.1088/1464-4258/9/8/s01
57. Robertson C, George SC Theory and Practical Recommendations for Autocorrelation-Based Image Correlation Spectroscopy. *J Biomed Opt* (2012) 17:080801. doi:10.1117/1.jbo.17.8.080801
58. Lee G, Leech G, Rust MJ, Das M, McGorty RJ, Ross JL, et al. Myosin-driven Actin-Microtubule Networks Exhibit Self-Organized Contractile Dynamics. *Sci Adv* (2021) 7:eabe4334. doi:10.1126/sciadv.abe4334
59. Sheung JY, Achiriloaie DH, Currie C, Peddireddy K, Xie A, Simon-Parker J, et al. Motor-driven Restructuring of Cytoskeleton Composites Leads to Tunable Time-Varying Elasticity. *ACS Macro Lett* (2021) 10:1151–8. doi:10.1021/acsmacrolett.1c00500
60. Schmidt FG, Hinner B, Sackmann E Microrheometry Underestimates the Values of the Viscoelastic Moduli in Measurements on F-Actin Solutions Compared to Macrorheometry. *Phys Rev E* (2000) 61:5646–53. doi:10.1103/physreve.61.5646
61. Davis JS Assembly Processes in Vertebrate Skeletal Thick Filament Formation. *Annu Rev Biophys Chem* (1988) 17:217–39. doi:10.1146/annurev.bb.17.060188.001245
62. Fisher CI, Kuo SC Filament Rigidity Causes F-Actin Depletion from Nonbinding Surfaces. *Proc Natl Acad Sci* (2009) 106:133–8. doi:10.1073/pnas.0804991106
63. Fitzpatrick R, Michieletto D, Peddireddy KR, Hauer C, Kyrillos C, Gurmessa BJ, et al. Synergistic Interactions between Dna and Actin Trigger Emergent Viscoelastic Behavior. *Phys Rev Lett* (2018) 121:257801. doi:10.1103/physrevlett.121.257801
64. Tang JX, Janmey PA The Polyelectrolyte Nature of F-Actin and the Mechanism of Actin Bundle Formation. *J Biol Chem* (1996) 271:8556–63. doi:10.1074/jbc.271.15.8556
65. Yu X, Carlsson AE Multiscale Study of Counterion-Induced Attraction and Bundle Formation of F-Actin Using an Ising-like Mean-Field Model. *Biophysical J* (2003) 85:3532–43. doi:10.1016/s0006-3495(03)74773-0

Conflict of Interest: The authors declare that the research was conducted in the absence of any commercial or financial relationships that could be construed as a potential conflict of interest.

Publisher's Note: All claims expressed in this article are solely those of the authors and do not necessarily represent those of their affiliated organizations, or those of the publisher, the editors and the reviewers. Any product that may be evaluated in this article, or claim that may be made by its manufacturer, is not guaranteed or endorsed by the publisher.

Copyright © 2021 Gurmessa, Rust, Das, Ross and Robertson-Anderson. This is an open-access article distributed under the terms of the Creative Commons Attribution License (CC BY). The use, distribution or reproduction in other forums is permitted, provided the original author(s) and the copyright owner(s) are credited and that the original publication in this journal is cited, in accordance with accepted academic practice. No use, distribution or reproduction is permitted which does not comply with these terms.